

**Bulk photovoltaic effect in hexagonal LuMnO<sub>3</sub> single crystals**Yunwei Sheng <sup>1</sup>, Ignasi Fina <sup>1,\*</sup>, Marin Gospodinov,<sup>2</sup> Aaron M. Schankler <sup>3</sup>,  
Andrew M. Rappe <sup>3</sup> and Josep Fontcuberta <sup>1,†</sup><sup>1</sup>*Institut de Ciència de Materials de Barcelona (ICMAB-CSIC), Campus UAB, Bellaterra 08193, Catalonia, Spain*<sup>2</sup>*Institute of Solid State Physics, Bulgarian Academy of Sciences, 1784 Sofia, Bulgaria*<sup>3</sup>*Department of Chemistry, University of Pennsylvania, Philadelphia, Pennsylvania 19104-6323, USA*

(Received 12 August 2021; revised 25 October 2021; accepted 3 November 2021; published 29 November 2021)

Hexagonal manganites, such as *h*-LuMnO<sub>3</sub>, are ferroelectric and have a narrow electronic band gap of  $\approx 1.5$  eV. Here we report on the photoresponse of *h*-LuMnO<sub>3</sub> single crystals. It is found that the short circuit photocurrent density ( $J_{sc}$ ) and the open circuit voltage ( $V_{oc}$ ) are dependent on the direction of the polarization plane of a linearly polarized impinging light. Its angular dependence indicates the contribution of bulk photovoltaic effect to the short circuit photocurrent. It is also observed that a switchable drift photocurrent, originating from the depoling field of the ferroelectric and thus tunable ( $<10\%$ ) by its polarization direction, also contributes to  $J_{sc}$ . Although its presence precludes accurate determination of the bulk photovoltaic tensor elements and Glass coefficients, some bounds can be established. The Glass coefficients are found to be significantly larger than those obtained in BiFeO<sub>3</sub>. We argue that the smaller band gap of *h*-LuMnO<sub>3</sub>, its distinctive bipyramidal crystal field, and electronic configuration ( $3d^4$  vs  $3d^5$ ), account for the difference and suggest a path towards ferroelectrics of higher photoconversion efficiency.

DOI: [10.1103/PhysRevB.104.184116](https://doi.org/10.1103/PhysRevB.104.184116)**I. INTRODUCTION**

Photoferroelectric materials are receiving new attention as efficient absorbers for photoelectric conversion. In conventional photovoltaic materials, photogenerated electron-hole pairs are driven out of the absorbing material by a built-in electric field, engineered by doping gradients (*p-n* junctions) and work function and electron affinity mismatch between different materials. In noncentrosymmetric materials photocarriers can be extracted from homogeneous materials, without any built-in electric field, with the additional advantage that the open circuit voltage is not limited by the band gap ( $E_g$ ) of the semiconducting absorber [1,2], with promises of higher efficiency. This is the so-called bulk photovoltaic effect (BPE) [3]. Ferroelectric materials fall within this category. Whereas the most common ferroelectrics, such as Pb(Zr, Ti)O<sub>3</sub> and BaTiO<sub>3</sub>, have a large band gap ( $\approx 3.6$  eV) and thus their photoabsorption in the visible range is rather limited, the discovery of a strong photoresponse in BiFeO<sub>3</sub> (BFO) ferroelectric with a narrower band gap (about 2.6–2.8 eV) constituted a hallmark that stimulated research on narrow gap photoferroelectrics [4–7]. The dependence of the short circuit photocurrent density ( $J_{sc}$ ) and open circuit voltage ( $V_{oc}$ ) on the polarization direction of the incoming light with respect to the crystal lattice [8] is commonly taken as a fingerprint of BPE, as identified in BFO [9,10]. Microscopic models have been developed to account for the BPE, and although still under some debate, have provided a rich insight,

emphasizing the important role of wave functions of excited states [11] and allowed some predictive guidance [12–15].

In BFO, the Fe<sup>3+</sup> ions have a  $3d^5$  electronic configuration and occupy an octahedral cage that breaks the degeneracy of the  $3d$  levels in basically two spin-up subsets  $t_{2g}$  and  $e_g$  that are fully electron occupied. Hexagonal *h*-RMnO<sub>3</sub> manganites, where R indicates a lanthanide (Sc-Lu), are room-temperature ferroelectrics with their polar axis along the hexagonal axis. The high spin trivalent Mn<sup>3+</sup> ions have a bipyramidal coordination and have a  $3d^4$  electronic configuration [16,17]. The different crystal-field symmetry and the different electronic occupation accounts for the semiconducting behavior and lower band gap of *h*-RMnO<sub>3</sub> (1.1–1.6 eV [18,19]). Importantly, the different nature of electronic ground and excited states in both materials anticipates a different BPE. The photoresponse of ferroelectric *h*-RMnO<sub>3</sub> thin films has been explored in some detail. It has been shown, for instance, that  $J_{sc}$  can be switched by reversing the ferroelectric polarization ( $P$ ) of the film, which indicates that the Schottky barriers at interfaces with electrodes play a major role [20]. However, to the best of our knowledge, no evidence of BPE has ever been reported neither in *h*-RMnO<sub>3</sub>, nor in the isostructural *h*-RFeO<sub>3</sub> [21,22]. Here we report on the photoresponse of *h*-LuMnO<sub>3</sub> (*h*-LMO) single crystals, aiming at determining its BPE response which may open new avenues beyond promising opportunities in conventional photovoltaics [23].

The ferroelectric  $P(E)$  loops of these crystals display a remanent room-temperature polarization of  $P_r \approx 7.3 \mu\text{C}/\text{cm}^2$  and the reported  $I(V)$  characteristics clearly indicate a photovoltaic response [24]. However, the conventional photoresponse and the bulk photovoltaic effect are intertwined, as shown in the following, and disentangling their relative

\*ifina@icmab.es

†fontcuberta@icmab.cat

contributions is challenging. On the basis of general grounds, it is first argued that in absorbing materials displaying anisotropic absorption and in the presence of built-in electric fields, as typically found in ferroelectric capacitors, the short circuit photocurrent may contain drift and diffusion terms ( $J_{\text{drift}}$ ,  $J_{\text{diff}}$ ) in addition to any BPE contribution ( $J_{\text{BPE}}$ ) [25]. Importantly, drift and diffusion photocurrent contributions may display a dependence on light polarization that manifests entanglement with BPE. It will be shown that *h*-LMO displays a remarkable  $J_{\text{sc}}$  and  $V_{\text{oc}}$  photoresponse both modulated by the polarization of the incoming light and its wavelength. It will be next argued that in the used experimental geometry, the diffusion term is negligible and it is shown that the observed dependence of the measured short circuit photocurrent on light polarization is mainly governed by BPE. However, we observe the presence of a drift-related photocurrent that also modulates  $J_{\text{sc}}$ . This contribution imposes bounds to the accuracy of the extracted Glass coefficients ( $G_{ij}$ ) and tensor element ( $\beta_{ij}$ ) of the BPE. The observed  $G_{ij}$  and  $\beta_{ij}$  values are found to be significantly larger than in BiFeO<sub>3</sub>. It is concluded that *h*-LMO displays a stronger responsiveness than rhombohedral ferrites and related materials, and we describe a scenario to account for the differences and possible avenues.

## II. EXPERIMENTAL METHODOLOGY

Single crystals of *h*-LuMnO<sub>3</sub> were grown by high-temperature flux technique. The crystals are hexagonal-shaped platelets, of thickness  $t \approx 100 \mu\text{m}$ , with the hexagonal  $c$  axis along the perpendicular to the largest faces. Crystals were chemically cleaned by using 6.5% HNO<sub>3</sub> solution to remove flux-growth residues from surfaces. Data on several crystals are reported here, named Cry-1, Cry-2, Cry-3, and Cry-4, all displaying similar features. Pt electrical contacts were grown at room temperature by RF sputtering. A stencil mask ( $\approx 58 \times 58 \mu\text{m}^2$ ) was used to create top Pt ( $\text{Pt}_{\text{top}} \approx 7 \text{ nm}$  thick) electrodes on Cry-1 and Cry-4, while a mask of a rectangular aperture was used to prepare a single top electrode on Cry-2 and Cry-3 with  $450 \mu\text{m} \times 270 \mu\text{m}$  and  $765 \mu\text{m} \times 480 \mu\text{m}$ , respectively. The optical transparency of 7 nm Pt in the used wavelength range, is of about 50% [26]. The bottom side of the *h*-LMO crystals was fully covered by a continuous Pt layer (7 nm thick) to be used as a bottom electrode ( $\text{Pt}_{\text{bot}}$ ). The crystals (Pt/*h*-LMO/Pt) were fixed on silicon substrates using silver paste.

The short circuit current density ( $J_{\text{sc}}$ ) dependence on light polarization angle ( $\varphi$ ) was recorded by a Keithley 6517B Electrometer. The  $V^{+/-}$  excitation was applied to the  $\text{Pt}_{\text{top}}$  electrode while the  $\text{Pt}_{\text{bot}}$  was grounded as sketched in Fig. 1(a), where positive current corresponds to positive charges flow towards  $\text{Pt}_{\text{bot}}$ . Data were recorded in dark or under illumination mainly using a blue-violet laser source ( $\lambda = 405 \text{ nm}$ ) of photon energy (3.06 eV), larger than the LMO band gap ( $E_g \approx 1.5 \text{ eV}$ ), and incidence power density within the  $0.6\text{--}27.6 \text{ W/cm}^2$  range. The spot diameter ( $S_d \approx 280 \mu\text{m}$ ) is much larger than the electrode size ( $\approx 58 \mu\text{m}$ ) and larger than the interelectrode distance ( $\approx 22 \mu\text{m}$ ) in Cry-1, allowing uniform top illumination of electrodes [Fig. 1(a)]. The angle of incidence of the light (wave vector  $\mathbf{k}$ ) (with respect to the normal to the sample plane

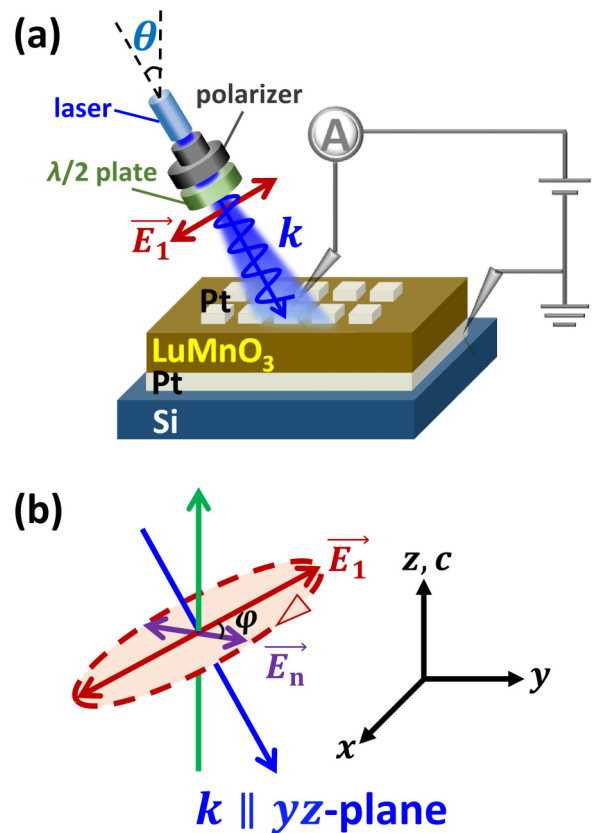


FIG. 1. (a) Photoresponse measurements under illumination of linearly polarized light at incidence angles  $\theta \approx 0^\circ\text{--}60^\circ$ . (b) Definition of the light linearly polarized angle  $\varphi$  (angle between  $\mathbf{E}_1$  and  $\mathbf{E}_n$ ), where the dashed ellipse indicates the rotation plane of the polarization vector, and the coordinate system is given by  $xyz$  with the  $z$  axis along the polar  $c$  axis of LMO. The blue arrows denote light propagation of wave vector  $\mathbf{k}$ . Red arrows denote the light polarization at  $\varphi = 0^\circ$  ( $\mathbf{E}_1$ , parallel with the incidence plane). Purple arrow represents the light polarization at intermediate angle ( $\mathbf{E}_n$ ).

direction) was varied between  $\theta \approx 0^\circ$  (normal incidence) and  $\approx 60^\circ$ . Dedicated experiments were also conducted for in-plane incidence ( $\theta \approx 90^\circ$ ) measurements, and cross-check experiments have been done to exclude spurious misalignment contributions. The photoresponse dependence on power and wavelength was recorded by using a STEC multiwavelength system (Blue Sky Research), with a parallel laser beam of  $\lambda = 405, 450, 520, \text{ and } 638 \text{ nm}$  (spot size  $\approx 2 \text{ mm}^2$ ,  $45^\circ$  incidence). The lasers were fed by a CPX400SA DC power source (AimTTi Co.). A polarizer and a half-wave ( $\lambda/2$ ) plate were used to obtain linearly polarized light and to rotate the polarization plane of the light ( $\mathbf{E}_n$ ) by angle  $\varphi$  [Fig. 1(b)]. At  $\varphi = 0^\circ$  the electric field of the light is in the incidence plane.

## III. RESULTS

Figures 2(a) and 2(b) show the short circuit photocurrent [ $J_{\text{sc}}(\theta, \varphi)$ ] and the open circuit photovoltage [ $V_{\text{oc}}(\theta, \varphi)$ ] measured along the  $z$  direction on a Pt/LMO/Pt sample (Cry-1), when varying the incidence angle ( $\theta$ ) and the polarization angle ( $\varphi$ ) of the light.

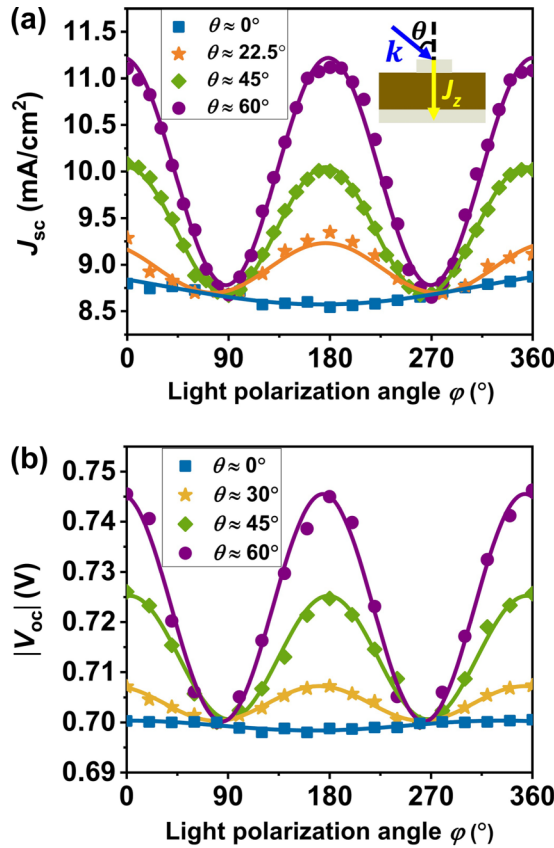


FIG. 2. Dependence of (a) short circuit current [ $J_{sc}(\theta, \varphi)$ ] and (b) the open circuit voltage [ $V_{oc}(\theta, \varphi)$ ], respectively, on the polarization angles ( $\varphi$ ) of the light at different incidence angles, of Cry-1. Solid lines are fits using Eq. (1) of experimental data (symbols). Light intensity  $I_0$  after optical plates and the top Pt is around  $15 \text{ W/cm}^2$ . The sketch illustrates the experimental arrangement. Notice that the illumination is through the top electrode.

Data indicate that  $J_{sc}(\theta, \varphi)$  and  $V_{oc}(\theta, \varphi)$  both display an oscillatory dependence on the polarization angle of light, being both maxima at  $\varphi = 0^\circ$ , which is when the  $\mathbf{E}$  electric field is in the incidence plane ( $p$  polarization), and minimum for  $\varphi = 90^\circ$  ( $s$  polarization).  $J_{sc}(\theta, \varphi)$  can be well described by

$$J_{sc}(\theta, \varphi) = A_z(\theta)\cos 2(\varphi - \varphi_0) + B_z(\theta), \quad (1)$$

where the  $A_z$  and  $B_z$  coefficients are related to incoming light intensity, absorption coefficient, and incidence angle, and may contain material-dependent parameters;  $\varphi_0 (< 4^\circ)$  is a phase shift that accounts for unavoidable instrumental misalignments. A similar expression holds for  $V_{oc}(\theta, \varphi)$ , as illustrated by the continuous line through data points in Fig. 2(b). In Fig. 2, the experimental variation occurring when changing the incidence angle are mitigated by a vertical shift of data collected at a different  $\theta$  angle, to make  $J_{sc}$  coincide at  $\varphi = 90^\circ$  with reference to  $J_{sc}(\theta = 90^\circ)$  (Supplemental Material S-1 [27]). It can be appreciated that the amplitude of the  $J_{sc}(\theta, \varphi)$  and  $V_{oc}(\theta, \varphi)$  oscillations varies with the incidence angle, being null at normal incidence and increasing when approaching grazing incidence. Therefore, data in Figs. 2(a) and 2(b) indicate that  $J_{sc}$  and  $V_{oc}$

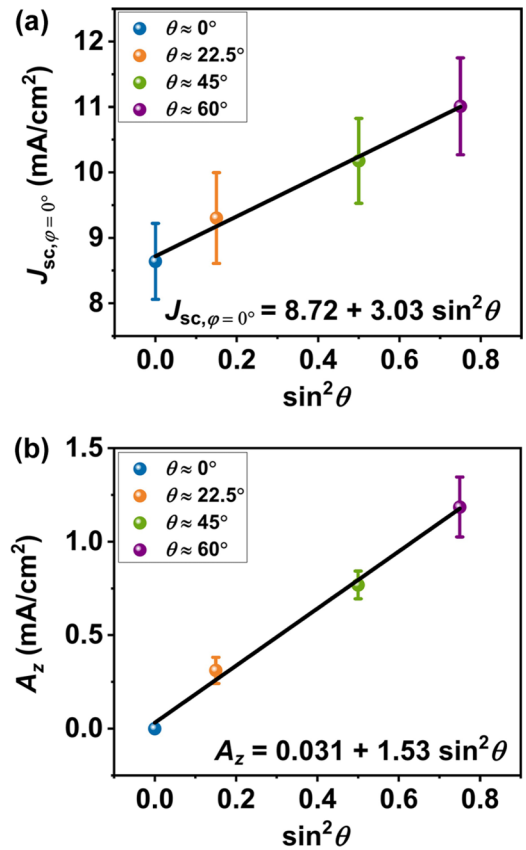


FIG. 3. Dependence of the (a) short circuit photocurrent recorded at  $\varphi = 0$  and (b) amplitude  $A_z(\theta)$  on  $\sin^2(\theta)$ , of Cry-1. Solid lines are linear fits of experimental data (symbols) as indicated. Error bars in figures indicate the spread of values (standard deviation, SD) from data recorded in six pads. Light intensity  $I_0$  after optical plates and the top Pt is around  $15 \text{ W/cm}^2$ .

both increase with the projection of  $\mathbf{E}_n$  along the  $z$  axis increasing.

This can be better seen in Fig. 3 displaying the dependence of  $J_{sc}(\theta, \varphi = 0^\circ)$  and the amplitude  $A_z(\theta)$  on the incidence angle. Moreover, it can be appreciated that  $A_z(\theta)$ ,  $B_z(\theta)$ , and consequently  $J_{sc}(\theta, \varphi = 0^\circ)$ , are all linear on  $\sin^2\theta$ .

Therefore, from data in Figs. 2 and 3 we conclude that

$$J_{sc}(\theta, \varphi) = A'_z \sin^2(\theta) \cos 2(\varphi - \varphi_0) + B'_z \sin^2(\theta) + C_z. \quad (2)$$

In order to understand the observed dependence of  $J_{sc}(\theta, \varphi)$  and  $V_{oc}(\theta, \varphi)$  on the polarization of light, we first note that the measured short circuit photocurrent ( $J_{sc}$ ) may contain contributions from drift ( $J_{\text{drift}}$ ) and diffusion ( $J_{\text{diff}}$ ) terms [25] and of bulk photovoltaic effect ( $J_{\text{BPE}}$ ):

$$J_{sc} \approx J_{\text{drift}} + J_{\text{diff}} + J_{\text{BPE}}. \quad (3)$$

It is well known that the bulk photovoltaic effect (BPE) gives rise to a genuine polarization dependence of  $J_{\text{BPE}}(\varphi)$ . Indeed, the observation of  $J_{sc}(\varphi)$  is commonly taken as a fingerprint of BPE. This assumption is well grounded in materials with weak photoabsorption ( $\alpha$ ) and in the absence of dichroism (i.e.,  $\alpha_x = \alpha_y = \alpha_z$ ), where observation of  $J_{\text{BPE}}(\varphi)$  can be safely attributed to BPE. However,  $h$ -LMO

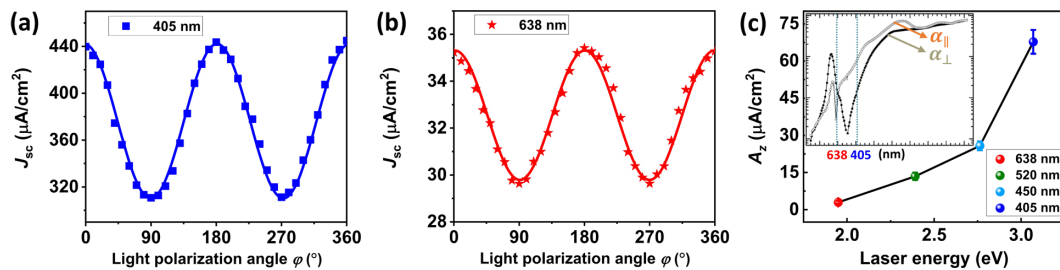


FIG. 4.  $J_{sc}(\varphi)$  at  $\theta \approx 45^\circ$  incidence (Cry-1) recorded at (a) 405 nm and (b) 638 nm, respectively. Solid lines are fits using Eq. (1) of experimental data (symbols). (c) Dependence of the amplitude  $A_z$  of the oscillations  $J_{sc}(\varphi)$  as a function of photon energy. Error bars in figures indicate the SD from data recorded in four junctions. Light intensity  $I_0$  after optical plates and the top Pt is around  $0.6 \text{ W/cm}^2$ . Note that absolute values of  $J_{sc}$  and  $A_z$  in (a)–(c) are smaller than in Fig. 2, due to the different laser fluency used in both cases ( $0.6$  and  $15 \text{ W/cm}^2$ , respectively). Inset in (c) is adapted from Ref. [29].

is known to be strongly absorbing at visible wavelengths and *h*-manganites are known to be dichroic ( $\alpha_{\perp} = \alpha_x = \alpha_y \neq \alpha_{\parallel} = \alpha_z$ , where the symbols “ $\perp$ ” and “ $\parallel$ ” indicate the direction perpendicular and parallel to  $z$  axis, respectively) [28–30]. In this case, polarization-dependent photoabsorption may give rise to polarization-dependent drift and diffusion terms [ $J_{\text{drift}}(\varphi)$ ,  $J_{\text{diff}}(\varphi)$ ] in the measured photocurrent [ $J_{sc}(\varphi)$ ].

In principle, owing to the geometry of the experiments in Fig. 1, the presence of interfacial electric fields, evident from the rectifying character of the measured  $I$ - $V$  (Supplemental Material S-2 [27]), shall give rise to  $J_{\text{drift}}$ . Moreover, the strong light absorption ( $\alpha \approx 5 \mu\text{m}^{-1}$ ) [29] at the upper surface of the crystal (attenuation length  $< 1 \mu\text{m}$ ) shall produce a gradient of photocarriers giving rise to a diffusion term  $J_{\text{diff}}$ . As mentioned, in the presence of dichroism, these two contributions will be entangled with any BPE response and observation of  $J_{sc}(\varphi)$  can no longer be taken as a fingerprint of BPE.

Aiming at disclosing if dichroism plays a relevant role on the polarization dependence observed in Figs. 2 and 3, we recorded  $J_{sc}(\varphi)$  at  $\theta = 45^\circ$  incidence for different wavelengths and inspected the variation of  $J_{sc}(\varphi)$  and then compared with the variations expected from the known dichroism ( $\alpha_{\parallel} \neq \alpha_{\perp}$ ) of *h*-AMO and its energy dependence. Although dichroism data of *h*-LMO is not available, optical measurements on isomorph *h*-YMnO<sub>3</sub> crystals [29] show that  $\Delta\alpha = \alpha_{\parallel} - \alpha_{\perp}$  strongly depends on light energy and  $\Delta\alpha$  changes its sign at about 2 eV. Accordingly, if dichroism were ruling the observed  $J_{sc}(\varphi)$ , one should expect that  $J_{sc}(E_{\parallel}) > J_{sc}(E_{\perp})$  and changing to  $J_{sc}(E_{\parallel}) < J_{sc}(E_{\perp})$  when using blue-violet (BV) or red (R) light, respectively, with their relative magnitudes dictated by  $\frac{\alpha_{\parallel}}{\alpha_{\perp}} \approx 4$  (BV) and  $\frac{\alpha_{\parallel}}{\alpha_{\perp}} \approx 0.2$  (R).

To test these predictions, we measured  $J_{sc}(\varphi)$  when illuminating the sample ( $\theta = 45^\circ$ ,  $0^\circ \leq \varphi \leq 360^\circ$ ) using different photon energies: 405 nm (3.06 eV) and 638 nm (1.95 eV). Data are displayed in Figs. 4(a) and 4(b). Data show the oscillations, as in Fig. 2, that can be similarly fitted using Eq. (1). Note that the background value and amplitude of the oscillations is smaller than in Fig. 2 due to the different laser source used in this experiment; here the laser intensity reaching the absorber is only of  $I_0 \approx 0.6 \text{ W/cm}^2$ . We have verified

that  $J_{sc}$  and the amplitude of the oscillations in the  $J_{sc}(\varphi)$  both increase with power fluency (not shown). We note that the observation of polarization-dependent oscillations when using in-plane illumination (see Fig. 5 below) excludes a significant contribution of the polarization-dependent reflectivity of the top electrode on the experimental results. Of relevance here is the observation that for blue-violet and red photons, the

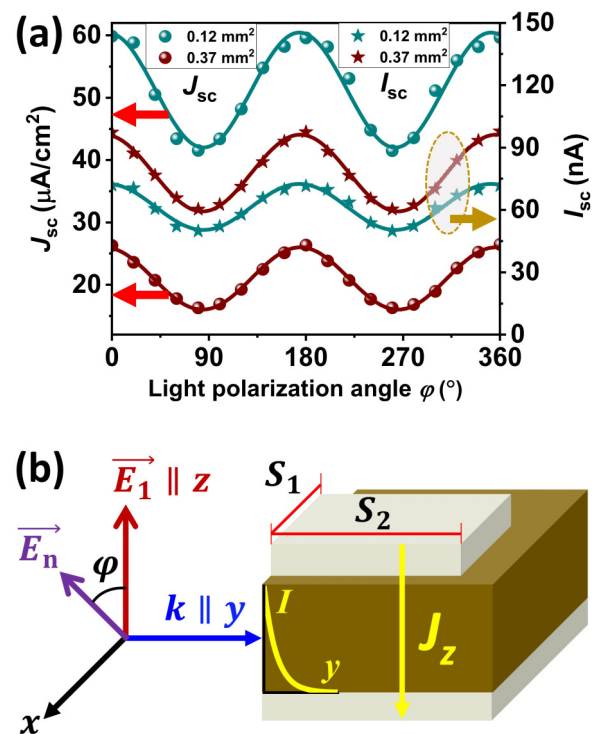


FIG. 5. (a) Left axis:  $J_{sc}(\varphi)$  (solid circles) measured at  $\theta \approx 90^\circ$  incidence using a top electrodes of area  $S_1 \times S_2 = 450 \mu\text{m} \times 270 \mu\text{m} = A_1 \approx 0.12 \text{ mm}^2$  (Cry-2) and  $S_1 \times S_2 = 770 \mu\text{m} \times 480 \mu\text{m} = A_2 \approx 0.37 \text{ mm}^2$  (Cry-3), placed up to the edge of the crystal surface. Right axis:  $I_{sc}(\varphi) = J_{sc}(\varphi) \times A$  (solid stars). Light intensity  $I_0$  after optical plates is around  $27.6 \text{ W/cm}^2$ . (b) Sketch of the experimental arrangement. The attenuation length of the light and the contact size ( $S_1$ ,  $S_2$ ) are indicated. In the sketch, the edge-electrode distance ( $D = 0$ ) is not shown.

photocurrent is always maximal at ( $\varphi = 0^\circ$ ), although obviously its magnitude depends on the photon energy. Indeed,  $J_{sc}(\varphi)$  in Fig. 4(a) changes by about 42% ( $\Delta J = \frac{J_{\varphi=0^\circ} - J_{\varphi=90^\circ}}{J_{\varphi=90^\circ}}$ ) when  $\varphi$  rotates from  $0^\circ$  to  $90^\circ$  when using blue-violet light but only about 19% [Fig. 4(b)] when using red light. These observations are in clear discordance with expectations from the dichroism of *h*-LMO and its energy dependence mentioned above. In fact, as shown in Fig. 4(c), the amplitude of  $J_{sc}(\varphi)$  is found to vary monotonically ( $\Delta J > 0$ ) with photon energy, which is not what should be expected from  $\alpha(\lambda)$  and  $\Delta\alpha(\lambda)$ . For convenience we include in Fig. 4(c) (inset) the anisotropic absorption  $\alpha(\lambda)$  reported for *h*-YMnO<sub>3</sub> [29]. Therefore, experimental data demonstrate that dichroism does not play a dominant role of the polarization dependence of  $J_{sc}(\varphi)$ . Consequently, in the following we analyze the  $J_{sc}(\theta, \varphi)$  data within the BPE scenario.

Within the BPE context,  $J_{BPE}$  is given by [8,10]

$$J_{BPE,i} = I_0 \cdot \alpha_{jk} \cdot G_{ijk} \cdot e_j e_k = I_0 \cdot \beta_{ijk} \cdot e_j e_k, \quad (4)$$

where  $J_{BPE,i}$  is the  $J_{BPE}$  along the  $i$  direction;  $I_0$  is the intensity of the light of given  $\lambda$ ;  $\alpha_{jk}$  is the absorption coefficients tensor;  $e_j, e_k$  are the projection of the incoming light polarization vector along the  $j, k$  direction, respectively;  $G_{ijk}$  and  $\beta_{ijk}(=\alpha_{jk}G_{ijk})$  are the Glass coefficients and the BPE tensor elements, respectively, that depend on the symmetry of the crystal centers, its electronic properties, and the photon energy [3,8]. In Eq. (4), the suffixes  $i, j, k$  represent  $x, y,$  and  $z$  axes in the Cartesian coordinate system for the electric field components of the incoming light; we take the  $z$  axis along the polar  $c$  axis of *h*-LMO.

For *h*-LMO [space group  $P6_3cm$ ; symmetry class  $6mm(\equiv C_{6v})$ ], the  $\beta_{ijk}$  tensor contains only three nonzero independent elements [31]. When using Eq. (4) to analyze data, it is commonly assumed that the absorption is weak and isotropic ( $\alpha_{jk} = \alpha$ ). We will first follow this simplifying assumption that will be released in a latter step. In this approximation and in the experimental arrangement (Fig. 1), the BPE [Eq. (4)] predicts an angular and polarization dependence of the short circuit photocurrent along the  $z$  axis given by (Supplemental Material S-3 [27])

$$J_{BPE} = I_0 \alpha \left( \frac{G_{33} - G_{31}}{2} \sin^2 \theta \cos 2\varphi + \frac{G_{33} - G_{31}}{2} \sin^2 \theta + G_{31} \right). \quad (5)$$

In the following  $\beta_{ij}$  and  $G_{ij}$  are written here in the conventional reduced matrix notation of the  $\beta_{ijk}$  and  $G_{ijk}$  tensors [32]. According to Eq. (5),  $J_{BPE}$  has a  $\cos(2\varphi)$  dependence on the light polarization, with an amplitude that depends on  $\sin^2(\theta)$ . Note that at normal incidence, BPE contributes to the photocurrent with a term independent on light polarization ( $J_{BPE} = I_0 \alpha G_{31}$ ). The angular dependence of  $J_{sc}$  in Figs. 2 and 4, as illustrated by the fitting functions Eqs. (1) and (2), closely follow predictions based on Eq. (5).

We also noted that the open circuit voltage  $V_{oc}(\theta, \varphi)$  [Fig. 2(b)] displays a cosinusoidal angular dependence, represented by Eq. (2) [ $V_{oc}(\theta, \varphi) \approx A(\theta) \cos 2\varphi + B(\theta) + C$ ] [solid lines through experimental data in Fig. 2(b)]. Within BPE,

$V_{oc}(\theta, \varphi)$  can be expressed by [9,33]

$$V_{oc} = \frac{J_{BPE} l}{\sigma_d + \sigma_{pv}}, \quad (6)$$

where  $\sigma_d$  and  $\sigma_{pv}$  are the dark and photo conductivity, respectively;  $l$  ( $\leq$  mean free path) is the effective thickness of the medium; and  $J_{BPE}$  is the current generated under short circuit conditions by BPE. Therefore, the angular dependence of  $V_{oc}(\varphi)$  should follow that of  $J_{BPE}$  as observed here. Hence, both  $J_{sc}(\theta, \varphi)$  and  $V_{oc}(\theta, \varphi)$  angular dependencies provide a strong indication that the BPE is ruling the light-polarization dependence of  $J_{sc}$ .

Finally, out-of-plane  $J_{sc}$  measurements have also been done at in-plane light incidence ( $\theta \approx 90^\circ$ ) by using dedicated samples (Cry-2 and Cry-3) and similar oscillation of  $J_{sc}(\varphi)$  are observed when rotating the light polarization angle. Figure 5(a) shows an illustrative example, data collected on Cry-2,3 using electrodes of area  $A_1 = 0.12 \text{ mm}^2$  and  $A_2 = 0.37 \text{ mm}^2$  placed just at the edge of the crystal surface. Data collected to exclude spurious misalignment contributions are included in the Supplemental Material S-4 [27]. Data in Fig. 5(a) display  $J_{sc}(\varphi)$  oscillations, similar to those observed at oblique incidence, reflecting how the photocurrent depends on the polarization direction of the light in relation to the crystalline axis [Fig. 5(b)].

All available data, particularly the in-plane incidence data, show that the out-of-plane photocurrent is maximal when the light polarization axis coincides ( $\varphi = 0^\circ$ ) with the optical axis of *h*-LMO. However, comparison of current density data collected at oblique incidence [Figs. 2(a) and 4(a)], with that obtained using in-plane incidence experiments [Fig. 5(a)], reveal two major differences. First, the collected photocurrent ( $I_{sc} = J_{sc} \times A$ ) is largely insensitive to contact area [Fig. 5(a), right axis]. As a matter of fact, as the illuminated spot size (diameter  $S_d \approx 280 \mu\text{m}$ ) is smaller than the lateral sizes of the electrode ( $S_1 \approx 450 \mu\text{m}$  for Cry-2 and  $770 \mu\text{m}$  for Cry-3), no additional current should be collected by increasing  $S_1$ , as illustrated by data in Fig. 5(a) (right axis). Consequently, it is observed in Fig. 5(a) (left axis) that the measured current density appears to depend on the contact area. Indeed, when reducing the contact area by about  $\approx 1/3 (= A_1/A_2)$ , the measured current density is not constant but increases by about a factor  $\approx 2.4$ . Moreover, out-of-plane  $J_{sc}$  recorded on Cry-4 using in-plane incidence measurements reduces and eventually vanishes when the collecting electrodes are placed at increasing distances ( $D$ ) from the crystal edge where light impinges the crystal and most of the photoabsorption takes place (Supplemental Material S-4 [27]). These observations indicate that: (a) photocarrier generation is limited to a narrow region at the edge of the crystal of depth  $\approx 1/\alpha < 1 \mu\text{m}$ , much smaller than the lateral size of the electrodes, and (b) recombination limits charge collection at distant electrodes [Fig. 5(b)]. Both effects indicate that derivation of Eq. (5) should be revised when photoabsorption is relevant.

Next task is to evaluate the Glass coefficients of *h*-LMO. Two sets of data are available to determine  $G_{33}$  and  $G_{31}$ : (a) data extracted at oblique incidence (Figs. 2 and 3), and (b) data collected from in-plane incidence (Fig. 5).

TABLE I. The photovoltaic tensor elements ( $\beta_{ij}$ ) and the Glass coefficients ( $G_{ij}$ ) of *h*-LuMnO<sub>3</sub>, evaluated in weak-absorbing (WA) and strong-absorbing limits (SA), from data collected at normal incidence and extrapolated grazing incidence. Data for BiFeO<sub>3</sub> and ZnO are also included. The corresponding absorption coefficients at the indicated wavelength ( $\lambda$ ) are indicated. The “ $\leq$ ” symbol in  $\beta_{ij}$  and  $G_{ij}$  data of LuMnO<sub>3</sub> indicates that  $J_{\text{drift}}$  contribution may be higher.

	S.G./S.C.	Method	$\beta_{ij}$ (kV <sup>-1</sup> )	$G_{ij}$ (pm/V)	$A$ ( $\mu\text{m}^{-1}$ )
LuMnO <sub>3</sub> ( $\lambda = 405$ nm)	<i>P6<sub>3</sub>cm/6mm</i>	Oblique incidence WA	$\beta_{31} \leq 0.581$ $\beta_{33} \leq 0.783$	$G_{31} \leq 116$ $G_{33} \leq 157$	$\approx 5$ [29]
		In-plane incidence SA	$\beta_{31} \leq 1.283$ $\beta_{33} \leq 8.744$	$G_{31} \leq 713$ $G_{33} \leq 1093$	$\alpha_{\perp} \approx 1.8$ [29] $\alpha_{\parallel} \approx 8$ [29]
ZnO ( $\lambda = 460$ nm)	<i>P6<sub>3</sub>cm/6mm</i>			$G_{31} \approx 2$ $G_{33} \approx 20$ [35]	0.0002 [35]
BiFeO <sub>3</sub> ( $\lambda = 405$ nm)	<i>R3c/3m</i>		$\beta_{15} \approx 0.05\text{--}0.07$ [9,12,36]	$G_{15} \approx 0.5\text{--}4$ [9,12]	6.04 [32]
			$\beta_{22} \approx 0.11\text{--}0.2$ [12,36]	$G_{22} \approx 4.5\text{--}7.8$ [10,12]	( $\lambda = 405$ nm)
			$\beta_{31} \approx 0.1\text{--}0.18$ [9,12,36]	$G_{31} \approx 6\text{--}6.5$ [9,12]	25 [10]
			$\beta_{33} \approx 0.1\text{--}0.3$ [9,12,36]	$G_{33} \approx 5\text{--}16$ [9,12]	( $\lambda = 435$ nm)

The photocurrent collected at oblique incidence, under the assumption of weak absorption, is given by

$$J_{\text{sc}} = J_{\text{BPE}} + J_{\text{drift}} + J_{\text{diff}}$$

$$= I_0 \alpha \left( \frac{G_{33} - G_{31}}{2} \sin^2 \theta \cos 2\varphi + \frac{G_{33} - G_{31}}{2} \sin^2 \theta + G_{31} \right) + J_{\text{drift}} + J_{\text{diff}}. \quad (7)$$

Using data in Figs. 3(a) and 3(b) and Eqs. (1) and (2) we deduce  $I_0 \alpha (G_{33} - G_{31}) \approx 3.03$  mA/cm<sup>2</sup> and  $I_0 \alpha G_{31} + J_{\text{drift}} + J_{\text{diff}} \approx 8.72$  mA/cm<sup>2</sup>.

Equation (7) emphasizes that in the presence of diffusion and drift terms, even in the absence of any dichroic absorption contribution, the  $G_{31}$  and  $G_{33}$  coefficients cannot be disentangled. However, as argued above, in the measuring configuration used here, the diffusion term can be neglected. Indeed, the penetration depth of visible light in LMO crystal ( $< 1$   $\mu\text{m}$ ) is much shorter than the crystal thickness ( $t \approx 100$   $\mu\text{m}$ ), and both lengths are expected to be large compared to the mean free path of carriers in LMO ( $< 1$   $\mu\text{m}$ ) [34]. We thus take  $J_{\text{diff}} \approx 0$ . Assuming  $J_{\text{diff}}$  and  $J_{\text{drift}}$  are both negligible, we obtain as upper bound values:  $G_{31} \approx 116$  pm/V and  $G_{33} \approx 157$  pm/V [ $I_0 \approx 15$  W/cm<sup>2</sup>,  $\alpha \approx 5$   $\mu\text{m}^{-1}$  (Table I)].

However, Eqs. (5) and (7) are appropriate to describe BPE contribution in weakly absorbing materials, where the light attenuation and its tensorial character are not relevant. Obviously this is not the case of *h*-LMO as dramatically shown by the in-plane incidence data in Fig. 5. In case of strongly absorbing and dichroic materials, derivation of appropriately modified  $J_{\text{sc}}(\theta = 90^\circ, \varphi)$  expression (along the  $z$  axis) for in-plane incidence (Supplemental Material S-5 [27]) leads to Eq. (8):

$$J_{\text{sc}} = \frac{I_0}{2S_2} \cdot \frac{S_d}{S_1} [(G_{33} - G_{31}) \cos 2\varphi + (G_{33} + G_{31})] + J_{\text{drift}}, \quad (8)$$

where  $S_d$  is the spot diameter;  $S_1, S_2$  is the length along the  $x, y$  axis of the electrode, respectively; and the  $J_{\text{diff}}$  is assumed again to be negligible. We note that Eq. (8) predicts that the current density decreases when increasing the length of the electrode, which is in agreement with the experimental evi-

dence in Fig. 5(a). Moreover, it follows from Eq. (8) that the measured current (and the current density) are independent on the absorption length ( $\approx 1/\alpha$ ), as far as  $S_2 \gg 1/\alpha$ , reflecting that all photoelectrons are created in a depth much smaller than the electrode size. Two limiting cases of Eq. (8) are of interest:

$$\text{At } \theta \approx 90^\circ; \quad \varphi = 0^\circ, \quad J_{\text{sc}} = \frac{I_0}{S_2} \cdot \frac{S_d}{S_1} \cdot G_{33} + J_{\text{drift}}, \quad (9a)$$

$$\text{At } \theta \approx 90^\circ; \quad \varphi = 90^\circ, \quad J_{\text{sc}} = \frac{I_0}{S_2} \cdot \frac{S_d}{S_1} \cdot G_{31} + J_{\text{drift}}, \quad (9b)$$

Using  $J_{\text{sc}}(\theta \approx 90^\circ; \varphi)$  data of Fig. 5, collected with the indicated two different electrodes [ $J_{\text{sc}}(\theta \approx 90^\circ; \varphi = 0^\circ, A_1) \approx 60$   $\mu\text{A}/\text{cm}^2$ ,  $J_{\text{sc}}(\theta \approx 90^\circ; \varphi = 90^\circ, A_1) \approx 42$   $\mu\text{A}/\text{cm}^2$ ,  $S_1 \approx 450$   $\mu\text{m}$ ,  $S_2 \approx 270$   $\mu\text{m}$  (Cry-2); and  $J_{\text{sc}}(\theta \approx 90^\circ; \varphi = 0^\circ, A_2) \approx 26$   $\mu\text{A}/\text{cm}^2$ ,  $J_{\text{sc}}(\theta \approx 90^\circ; \varphi = 90^\circ, A_2) \approx 16$   $\mu\text{A}/\text{cm}^2$ ,  $S_1 \approx 770$   $\mu\text{m}$ ,  $S_2 \approx 480$   $\mu\text{m}$  (Cry-3);  $I_0 \approx 27.6$  W/cm<sup>2</sup>,  $S_d \approx 280$   $\mu\text{m}$ ], we obtain (upper bounds, assuming  $J_{\text{drift}} \approx 0$ ):  $G_{31} \approx 660\text{--}765$  pm/V and  $G_{33} \approx 943\text{--}1243$  pm/V. The corresponding average values are:  $G_{31} \approx 713 \pm 53$  pm/V and  $G_{33} \approx 1093 \pm 150$  pm/V. As expected, the Glass coefficients obtained using the strong absorption limit are larger than those obtained above under the weak-absorption condition. In Table I we include the Glass coefficients  $G_{ij}$  together with the corresponding BPE tensor elements  $\beta_{ij}$  deduced in the weak-absorbing (WA) and strong-absorbing (SA) cases.

We address in the following the contribution of  $J_{\text{drift}}$  to the measured  $J_{\text{sc}}$ , that we have so far neglected. We first note that  $J_{\text{drift}}$  is related to the presence of internal electric fields (depolarizing) and others (imprint, etc.) that give rise to a switchable  $J_{\text{drift}}$  contribution (denoted here  $J_{\text{drift,SW}}$ ) and a nonswitchable component respectively (denoted here  $J_{\text{drift,NSW}}$ ) as discussed in Ref. [24]. The  $J_{\text{drift,SW}}$  contribution can be evaluated by performing and comparing  $J_{\text{sc}}$  measurements after prepolarizing the sample up or down. With this aim we recorded  $J_{\text{sc}}(\theta, \varphi)$  as a function of the ferroelectric polarization ( $P$ ) state of the sample to unravel the contribution of the depolarizing field  $E_d$  to  $J_{\text{sc}}$ . A unipolar prepolarizing voltage ( $V_{w,\text{max}} > V_c$  coercive voltage) of different sign was applied to the top Pt electrode

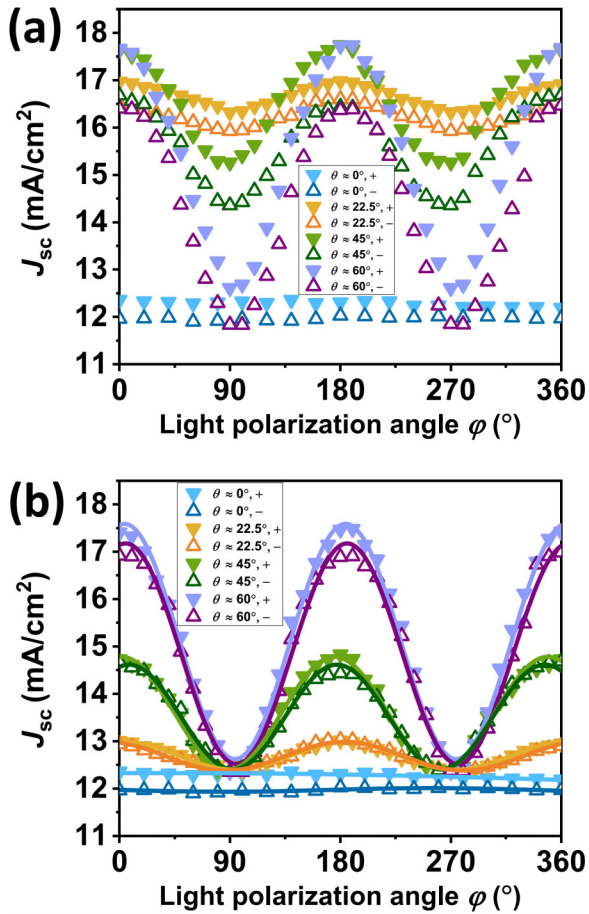


FIG. 6. Dependence of short circuit photocurrent  $J_{sc}(\theta, \varphi)$  on the polarization of light ( $\varphi$ ), at various incidence angles ( $\theta$ ), of Cry-1 at prepolarized to  $P$ -down and  $P$ -up states using ( $V_w^+/V_w^- = \pm 150$  V). Signs “+” and “-” signify positive and negative prepolarizing voltage. Solid lines are fits using Eq. (1) to experimental data (symbols). Light intensity  $I_0$  after optical plates and the top Pt is around  $22.5$  W/cm $^2$ . Data for  $J_{sc}(\theta \neq 0^\circ, \varphi)$  have been vertically shifted such as  $J_{sc}(\theta \neq 0^\circ, \varphi = 90^\circ)$  to coincide with  $J_{sc}(\theta \neq 0^\circ, \varphi = 90^\circ; V_w^+ = +150$  V).

with a duration of  $\approx 50$  s, which is long enough to saturate the polarization of the sample [ $P(E)$  loops were measured at 1 kHz] [24]. After a dwell time  $\tau_d = 5$  s, the short circuit photocurrent was recorded at various light polarization direction ( $\varphi$ ) and incidence angle ( $\theta$ ). In Fig. 6(a) we show the raw  $J_{sc}$  data recorded as a function of  $\theta$  and  $\varphi$  and measured after prepolarizing the sample (Cry-1) with  $V_w = \pm 150$  V. Data for  $\theta = 0^\circ$  most clearly illustrate the dependence of  $J_{sc}$  on polarization direction, as expected in the presence of  $J_{\text{drift,SW}}$ , that modulates  $J_{sc}$  being  $J_{sc}$  slightly larger for  $V_w^+$  ( $P$ -down) than for  $V_w^-$  ( $P$ -up) polarization. The same trend can be appreciated by any  $\theta$ .

At normal incidence, the polarization vector of light is perpendicular to the ferroelectric polarization ( $P||z$ ) and  $J_{sc}$  varies by about 3% upon polarization reversal. When increasing the incidence angle ( $\theta$ ), that is when increasing the component of the light polarization along the  $z$  axis, the  $P$  dependence of the photocurrent slightly differs (3%–6%), although being in all cases somewhat larger in  $P$ -down than in

$P$ -up. This difference is a signature of a switchable  $J_{\text{drift,SW}}$  term, that at remanence and depending on the direction of ferroelectric polarization, affects the internal electric field in  $h$ -LMO and thus  $J_{sc}$ . As already reported, polarization-modulated Schottky barriers at  $h$ -LMO/electrode interfaces [24] allow us to modulate the photocurrent upon  $P$  switching. As observed, at remanence,  $J_{sc}$  is modified by less than 10%, and thus the BPE coefficient extracted using Eqs. (7) and (8) above is only accurate within 10%.

To discern any possible effect of the polarization direction on the amplitude of the  $J_{sc}(\theta, \varphi)$  oscillations, while minimizing experimental artifacts occurring when changing the incidence angle, the raw of Fig. 6(a) has been normalized, as in Fig. 2, by a vertical shift to coincide at  $\varphi = 90^\circ$  with  $J_{sc}(\theta = 0^\circ, \varphi = 90^\circ)$  data collected at  $V_w = +150$  V and shown in Fig. 6(b). It appears that the amplitude of the  $J_{sc}(\varphi)$  oscillations are also slightly modulated by the polarization direction. However, available data does not allow us to discern if this variation is genuine or results from spurious effects.

In summary, the switchable component of the drift photocurrent ( $J_{\text{drift,SW}}$ ) is only about 3%–6% of the measured  $J_{sc}$ . It follows that the photocurrent in these LuMnO $_3$  crystals is governed by the contributions of  $J_{\text{BPE}}$  and  $J_{\text{drift,NSW}}$ . At normal incidence both contributions cannot be disentangled and thus  $J_{\text{BPE}}$  can be any value within (0%–100%) of  $J_{sc}$ . However, at oblique incidence the observation of obvious oscillations, depending on the polarization angles, allows us to set minimal values for  $J_{\text{BPE}}$  that reaches up to 34% at grazing incidence (Supplemental Material S-6 [27]).

We end by comparing the Glass coefficients ( $G_{ij}$ ) and the corresponding tensor elements ( $\beta_{ij} = \alpha_{jk} G_{ij}$ ) of  $h$ -LMO determined above (summarized in Table I) with the corresponding data reported in the weakly absorbing and isostructural ZnO and in the intensively studied strongly absorbing BiFeO $_3$ . It can be appreciated in Table I that the Glass coefficients of  $h$ -LMO, having the same symmetry class as ZnO, are much larger. This fact is likely related to the different nature of valence and conduction bands and the corresponding optical transitions. Being the symmetry classes of  $h$ -LMO and  $r$ -BiFeO $_3$  different ( $6mm$  and  $3m$ , respectively), the corresponding tensor elements cannot be easily compared. However, the observation of larger  $\beta_{ij}$  and  $G_{ij}$  values in  $h$ -LMO than in BiFeO $_3$  reflects the important role of the trigonal and octahedral crystal field splitting setting the corresponding excited states and their impact on BPE.

#### IV. SUMMARY AND CONCLUSIONS

We have measured the photoresponse of ferroelectric  $h$ -LuMnO $_3$  crystals along the hexagonal  $c$  axis using Pt electrodes, using oblique and in-plane light incidence. The analysis of the dependence of  $J_{sc}$  on the polarization direction of the incoming light and its incidence angle  $J_{sc}(\theta, \varphi)$  have provided consistent data revealing a clear contribution arising from BPE. It turns out that  $J_{sc}$  is the largest when the polarization axis of the light is parallel to the polar hexagonal axis. Short circuit photoresponse measurements using in-plane light incidence have also provide evidence of the impact of the strong optical absorption on the out-of-plane

photocurrent density, most noticeable in the inverse dependence on the electrode area. The presence of contributions to  $J_{sc}$  that do not originate from BPE but are related to drift currents implies that only bounds for the Glass coefficients and tensor elements can be given. In spite of these caveats, the BPE coefficients  $\beta_{ij}$  and  $G_{ij}$  are significantly larger than other photoferroelectrics, such as BiFeO<sub>3</sub>, suggesting possible advantages for photoconversion.

### ACKNOWLEDGMENTS

Financial support from the Spanish Ministry of Science, Innovation and Universities, through the “Severo Ochoa” Programme for Centers of Excellence in R&D (FUNFUTURE CEX2019-000917-S), PID2020-118479RB-I00 (AEI/FEDER, EU) (AEI/FEDER, EU), and PID2019-

107727RB-I00 (AEI/FEDER, EU) projects, and from Generalitat de Catalunya (2017 SGR 1377) is acknowledged. I.F. acknowledges RyC Contract RYC-2017-22531. Project supported by a 2020 Leonardo Grant for Researchers and Cultural Creators, BBVA Foundation. The theoretical component of this work (A.M.S. and A.M.R.) was supported by the U.S. Department of Energy, Office of Science, Basic Energy Sciences, under Award No. DE-FG02-07ER46431. Computational support was provided by the National Energy Research Scientific Computing Center (NERSC), a U.S. Department of Energy, Office of Science User Facility located at Lawrence Berkeley National Laboratory, operated under Contract No. DE-AC02-05CH11231. The experimental and theoretical contributions of Y.S. are financially supported by China Scholarship Council (CSC), respectively with No. 201806410010. The work of Y.S. has been done as a part of her Ph.D. program in Materials Science at Universitat Autònoma de Barcelona.

- 
- [1] A. M. Glass, D. von der Linde, and T. J. Negran, High-voltage bulk photovoltaic effect and the photorefractive process in LiNbO<sub>3</sub>, *Appl. Phys. Lett.* **25**, 233 (1974).
- [2] W. T. H. Koch, R. Munser, W. Ruppel, and P. Würfel, Bulk photovoltaic effect in BaTiO<sub>3</sub>, *Solid State Commun.* **17**, 847 (1975).
- [3] V. M. Fridkin and B. N. Popov, Anomalous photovoltaic effect in ferroelectrics, *Usp. Fiz. Nauk* **126**, 657 (1978) [*Sov. Phys. Usp.* **21**, 981 (1978)].
- [4] T. Choi, S. Lee, Y. J. Choi, V. Kiryukhin, and S.-W. Cheong, Switchable ferroelectric diode and photovoltaic effect in BiFeO<sub>3</sub>, *Science* **324**, 63 (2009).
- [5] S. Y. Yang, J. Seidel, S. J. Byrnes, P. Shafer, C.-H. Yang, M. D. Rossell, P. Yu, Y.-H. Chu, J. F. Scott, J. W. Ager, L. W. Martin, and R. Ramesh, Above-bandgap voltages from ferroelectric photovoltaic devices, *Nat. Nanotechnol.* **5**, 143 (2010).
- [6] R. Nechache, C. Harnagea, S. Li, L. Cardenas, W. Huang, J. Chakrabarty, and F. Rosei, Bandgap tuning of multiferroic oxide solar cells, *Nat. Photonics* **9**, 61 (2015).
- [7] L. You, F. Zheng, L. Fang, Y. Zhou, L. Z. Tan, Z. Zhang, G. Ma, D. Schmidt, A. Rusydi, L. Wang, L. Chang, A. M. Rappe, and J. Wang, Enhancing ferroelectric photovoltaic effect by polar order engineering, *Sci. Adv.* **4**, eaat3438 (2018).
- [8] B. Sturman and V. M. Fridkin, *The Photovoltaic and Photorefractive Effects in Noncentrosymmetric Materials* (Gordon and Breach, Philadelphia, 1992).
- [9] A. Bhatnagar, A. Roy Chaudhuri, Y. Heon Kim, D. Hesse, and M. Alexe, Role of domain walls in the abnormal photovoltaic effect in BiFeO<sub>3</sub>, *Nat. Commun.* **4**, 2835 (2013).
- [10] W. Ji, K. Yao, and Y. C. Liang, Evidence of bulk photovoltaic effect and large tensor coefficient in ferroelectric BiFeO<sub>3</sub> thin films, *Phys. Rev. B* **84**, 094115 (2011).
- [11] B. M. Fregoso, T. Morimoto, and J. E. Moore, Quantitative relationship between polarization differences and the zone-averaged shift photocurrent, *Phys. Rev. B* **96**, 075421 (2017).
- [12] S. M. Young, F. Zheng, and A. M. Rappe, First-Principles Calculation of the Bulk Photovoltaic Effect in Bismuth Ferrite, *Phys. Rev. Lett.* **109**, 236601 (2012).
- [13] L. Z. Tan, F. Zheng, S. M. Young, F. Wang, S. Liu, and A. M. Rappe, Shift current bulk photovoltaic effect in polar materials—Hybrid and oxide perovskites and beyond, *Npj Comput. Mater.* **2**, 16026 (2016).
- [14] R. Fei, W. Song, and L. Yang, Giant photogalvanic effect and second-harmonic generation in magnetic axion insulators, *Phys. Rev. B* **102**, 035440 (2020).
- [15] B. I. Sturman, Ballistic and shift currents in the bulk photovoltaic effect theory, *Phys.-Usp.* **63**, 407 (2020).
- [16] J. Fontcuberta, Multiferroic RMnO<sub>3</sub> thin films, *C. R. Phys.* **16**, 204 (2015).
- [17] B. Lorenz, Hexagonal manganites—(RMnO<sub>3</sub>): Class (I) multiferroics with strong coupling of magnetism and ferroelectricity, *ISRN Condens. Matter Phys.* **2013**, 497073 (2013).
- [18] C. Degenhardt, M. Fiebig, D. Fröhlich, T. Lottermoser, and R. V. Pisarev, Nonlinear optical spectroscopy of electronic transitions in hexagonal manganites, *Appl. Phys. B* **73**, 139 (2001).
- [19] W. Wang, H. Wang, X. Xu, L. Zhu, L. He, E. Wills, X. Cheng, D. J. Keavney, J. Shen, X. Wu, and X. Xu, Crystal field splitting and optical bandgap of hexagonal LuFeO<sub>3</sub> films, *Appl. Phys. Lett.* **101**, 241907 (2012).
- [20] H. Han, S. Song, J. H. Lee, K. J. Kim, G.-W. Kim, T. Park, and H. M. Jang, Switchable photovoltaic effects in hexagonal manganite thin films having narrow band gaps, *Chem. Mater.* **27**, 7425 (2015).
- [21] H. Han, D. Kim, K. Chu, J. Park, S. Y. Nam, S. Heo, C.-H. Yang, and H. M. Jang, Enhanced switchable ferroelectric photovoltaic effects in hexagonal ferrite thin films via strain engineering, *ACS Appl. Mater. Interfaces* **10**, 1846 (2018).
- [22] H. Han, D. Kim, S. Chae, J. Park, S. Y. Nam, M. Choi, K. Yong, H. J. Kim, J. Son, and H. M. Jang, Switchable Ferroelectric photovoltaic effects in epitaxial *h*-RFeO<sub>3</sub> thin films, *Nanoscale* **10**, 13261 (2018).
- [23] X. Huang, T. R. Paudel, S. Dong, and E. Y. Tsymbal, Hexagonal rare-earth manganites as promising photovoltaics and light polarizers, *Phys. Rev. B* **92**, 125201 (2015).
- [24] Y. Sheng, I. Fina, M. Gospodinov, and J. Fontcuberta, Switchable photovoltaic response in hexagonal LuMnO<sub>3</sub> single crystals, *Appl. Phys. Lett.* **118**, 232902 (2021).

- [25] P. Würfel, *Physics of Solar Cells* (Wiley, New York, 2005).
- [26] M. N. Polyanskiy, Refractive Index Database, <https://refractiveindex.info/>. (accessed on May 3, 2021).
- [27] See Supplemental Material at <http://link.aps.org/supplemental/10.1103/PhysRevB.104.184116> for the normalization of angular dependence, the rectifying behavior in dark, the derivation of equations at WA and SA incidence, and the measurements with top electrode capped and placed at different edge distance at in-plane incidence, which includes Ref. [37].
- [28] A. F. Lima and M. V. Lalic, Optical absorption spectrum and electronic structure of multiferroic hexagonal YMnO<sub>3</sub> compound, *Opt. Mater. (Amst.)* **64**, 406 (2017).
- [29] R. Schmidt-Grund, S. Richter, S. G. Ebbinghaus, M. Lorenz, C. Bundesmann, and M. Grundmann, Electronic Transitions and dielectric function tensor of a YMnO<sub>3</sub> single crystal in the NIR-VUV spectral range, *RSC Adv.* **4**, 33549 (2014).
- [30] A. M. Kalashnikova and R. V. Pisarev, Electronic structure of hexagonal rare-earth manganites RMnO<sub>3</sub>, *J. Exp. Theor. Phys. Lett.* **78**, 143 (2003).
- [31] M. de Jong, W. Chen, H. Geerlings, M. Asta, and K. A. Persson, A database to enable discovery and design of piezoelectric materials, *Sci. Data* **2**, 150053 (2015).
- [32] S. Nakashima, K. Takayama, T. Uchida, H. Fujisawa, and M. Shimizu, Anomalous photovoltaic effects in Pt/single-domain-structured BiFeO<sub>3</sub>/Pt coplanar capacitors on SrTiO<sub>3</sub> substrates, *Jpn. J. Appl. Phys.* **54**, 10NA16 (2015).
- [33] V. M. Fridkin, *Photoferroelectrics* (Springer, Berlin, 1979), Vol. 9.
- [34] L. Wang, Y. Li, A. Bera, C. Ma, F. Jin, K. Yuan, W. Yin, A. David, W. Chen, W. Wu, W. Prellier, S. Wei, and T. Wu, Device Performance of the Mott Insulator LaVO<sub>3</sub> as a Photovoltaic Material, *Phys. Rev. Appl.* **3**, 064015 (2015).
- [35] V. M. Fridkin, E. P. Efremova, B. H. Karimov, V. A. Kuznezov, I. P. Kuzmina, A. N. Lobachev, V. G. Lazarev, and A. J. Rodin, The experimental investigation of the photovoltaic effect in some crystals without a center of symmetry, *Appl. Phys.* **25**, 77 (1981).
- [36] M.-M. Yang, A. Bhatnagar, Z.-D. Luo, and M. Alexe, Enhancement of local photovoltaic current at ferroelectric domain walls in BiFeO<sub>3</sub>, *Sci. Rep.* **7**, 43070 (2017).
- [37] S. H. Skjærø, E. T. Wefring, S. K. Nesdal, N. H. Gaukås, G. H. Olsen, J. Glaum, T. Tybell, and S. M. Selbach, Interstitial oxygen as a source of p-type conductivity in hexagonal manganites, *Nat. Commun.* **7**, 13745 (2016).